

Accelerated Meshfree Method for Metal Forming Simulation

Sangpil Yoon¹ and Jiun-Shyan Chen²

Department of Civil & Environmental Engineering

University of California, Los Angeles

5731G Boelter Hall

Los Angeles, CA 90095-15

Finalist of 13th ROBERT J. MELOSH MEDAL COMPETITION FOR THE BEST STUDENT
PAPER ON FINITE ELEMENT ANALYSIS, 2001

Invited for Publication in a Special Issue of Journal of Finite Element Analysis & Design

November, 2001

¹ Postdoctoral Fellow, Department of Civil & Environmental Engineering, University of California, Los Angeles, 5731G Boelter Hall, Los Angeles, Los Angeles, CA 90095-1593.

² Corresponding author, Associate Professor, Department of Civil & Environmental Engineering, University of California, Los Angeles, 5731G Boelter Hall, Los Angeles, Los Angeles, CA 90095-1593. E-mail: jschen@seas.ucla.edu

ABSTRACT

An accelerated meshfree method based on a stabilized conforming nodal integration (SCNI) method is developed for elastoplastic contact analysis of metal forming processes. In this approach, strain smoothing stabilization is introduced to eliminate spatial instability in Galerkin meshfree methods when the weak form is integrated by a nodal integration. The gradient matrix associated with strain smoothing satisfies the integration constraint for linear exactness in the Galerkin approximation. Strain smoothing formulation and numerical procedures for path-dependent problems are introduced. Applications to metal forming analysis are presented, with results demonstrating a significant improvement in computational efficiency without loss of accuracy.

Key words: meshfree methods, stabilized conforming nodal integration, metal forming, reproducing kernel, integration constraints

1. INTRODUCTION

Gauss integration is commonly used in Galerkin based meshfree methods [1, 3, 10, 11]. Although the growing body of research in meshfree methods demonstrates the effectiveness of these methods to address large deformation and complex contact conditions [6], the high CPU cost of the Galerkin-based meshfree method remains problematic. The high computational effort in meshfree methods primarily results from stiffness matrix evaluation and solution of the dense matrix in the linear algebraic equations. Other issues associated with Gauss integration are (1) a specialized integration zone pattern required for non uniform node distribution [4], and (2) the failure of Gauss integration to satisfy linear exactness in the Galerkin approximation (integration constraints) with non uniform discretization [7].

A stabilized conforming nodal integration (SCNI) method has been employed to reduce computational cost in stiffness evaluation [7]. In this approach, a strain smoothing stabilization has been implemented as a means to meet integration constraints and to provide a stabilization for nodal integration. SCNI not only yields a significant reduction in computational cost, it can also achieve a higher accuracy [7] due to the satisfaction of integration constraints. This paper discusses the extension of SCNI to history-dependent problems with applications to metal forming problems.

This paper is organized as follows. Section 2 provides the review of SCNI for linear elasticity. The extension of SCNI to path-dependent nonlinear problems is presented in Section 3. Several metal forming problems are demonstrated in Section 4, and concluding remarks are given in Section 5.

2. STABILIZED CONFORMING NODAL INTEGRATION

2.1 Meshfree Shape Function

The approximation methods most widely used in meshfree methods are the moving least-squares (MLS) approximation [10], partition of unity method (PUM) [1,3], and the reproducing kernel (RK) approximation [11]. Without loss of generality, the MLS and RK approximation for construction of the meshfree shape function is introduced in this section. The reproducing MLS-RK approximation of a variable $u(\mathbf{x})$, denoted by $u^h(\mathbf{x})$, is

$$u^h(\mathbf{x}) = \sum_{I=1}^{NP} \Psi_I(\mathbf{x}) u_I \quad (1)$$

$$\Psi_I(\mathbf{x}) = \mathbf{H}^T(0) \mathbf{M}^{-1}(\mathbf{x}) \mathbf{H}(\mathbf{x} - \mathbf{x}_I) \Phi_{a_I}(\mathbf{x} - \mathbf{x}_I) \quad (2)$$

$$\mathbf{M}(\mathbf{x}) = \sum_{I=1}^{NP} \mathbf{H}(\mathbf{x} - \mathbf{x}_I) \mathbf{H}^T(\mathbf{x} - \mathbf{x}_I) \Phi_{a_I}(\mathbf{x} - \mathbf{x}_I) \quad (3)$$

where $\Phi_{a_I}(\mathbf{x} - \mathbf{x}_I)$ is a kernel function with compact support “ a ”, u_I is the coefficient of approximation (generally not a nodal value), $\mathbf{H}^T(\mathbf{x} - \mathbf{x}_I) = \{1, x_1 - x_{1I}, x_2 - x_{2I}, \dots, (x_3 - x_{3I})^n\}$ is the vector of monomial basis, NP is the number of particles, and $\Psi_I(\mathbf{x})$ is the meshfree shape function. A meshfree shape function and domain discretization is illustrated in Fig. 1. This meshfree shape function was constructed based on reproducing conditions and therefore is capable of exactly representing n -th order monomials (n -th order consistency):

$$\sum_{I=1}^{NP} \Psi_I(\mathbf{x}) x_{1I}^i x_{2I}^j x_{3I}^k = x_1^i x_2^j x_3^k; \quad 0 \leq i + j + k \leq n \quad (4)$$

The meshfree Galerkin approximation is formulated by introducing meshfree shape functions, e.g., Eq. (2), into the weak form. Gauss integration is usually used in the integration of

the weak form [3]. It has become apparent that shortcomings exist with respect to Gauss integration for Galerkin meshfree methods. Using Gauss integration, domain partitioning must match the shape function supports to minimize integration error [4]. The higher order Gauss integration required for meshfree computation is computationally inefficient. Further, Gauss integration does not meet linear exactness in the Galerkin meshfree approximation [7], as discussed in the following.

2.2 Integration Constraints and Strain Smoothing Stabilization

To obtain linear exactness in the Galerkin approximation, a discrete linear displacement must exactly satisfy the discrete equilibrium equation of a boundary value problem in which the solution is linear. Linear exactness in Galerkin approximation first requires linear consistency in the MLS-RK approximation. Second, numerical integration of stiffness and force must meet the following condition for interior nodes [7]:

$$\sum_{L=1}^{NIT} \mathbf{B}_I(\mathbf{x}_L) \omega_L = \mathbf{0}; \quad \text{for all interior nodes } \{I: \text{supp}(\Psi_I) \cap \Gamma = \emptyset\} \quad (5)$$

where \mathbf{B}_I is the gradient matrix associated with node I , Γ is the total boundary, \mathbf{x}_L is the integration points, ω_L is the weight, and NIT is the number of integration points. For shape functions intersect with essential boundary, flux equilibrium is required [7].

Strain smoothing stabilization has been proposed [7] to achieve two objectives: (1) to avoid taking derivatives at nodal points for stability, and (2) to construct a modified gradient matrix that satisfies the integration constraints in Eq. (5). A strain smoothing equation has been proposed by [7] as:

$$\tilde{\boldsymbol{\varepsilon}}_{ij}^h(\mathbf{x}_L) = \frac{1}{A_L} \int_{\Omega_L} \boldsymbol{\varepsilon}_{ij}^h d\Omega = \frac{1}{2A_L} \int_{\Omega_L} \left(\frac{\partial u_i^h}{\partial x_j} + \frac{\partial u_j^h}{\partial x_i} \right) d\Omega = \frac{1}{2A_L} \int_{\Gamma_L} (u_i^h n_j + u_j^h n_i) d\Gamma \quad (6)$$

Introducing shape function for displacement into Eq. (6) leads to

$$\tilde{\boldsymbol{\varepsilon}}^h(\mathbf{x}_L) = \sum_{I \in G_L} \tilde{\mathbf{B}}_I(\mathbf{x}_L) \mathbf{d}_I \quad (7)$$

where $\tilde{\boldsymbol{\varepsilon}}^h$ is the smoothed strain, $\boldsymbol{\varepsilon}^h_{ij}$ is the strain obtained from displacement by compatibility, $\boldsymbol{\varepsilon}^h_{ij} = (u^h_{i,j} + u^h_{j,i})/2$, Ω_L and Γ_L are the representative domain and boundary, respectively, of node L obtained from, for example, the Voronoi diagram in Fig. 2, and A_L is the area (or volume) of Ω_L . It can be shown that the smoothed gradient matrix $\tilde{\mathbf{B}}_I$ satisfies the integration constraints in Eq. (5). The convergence study has been presented in [7].

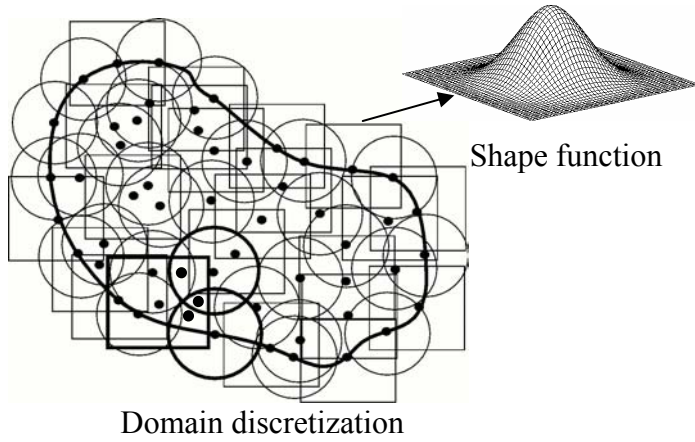


Figure 1 Meshfree discretization and shape function

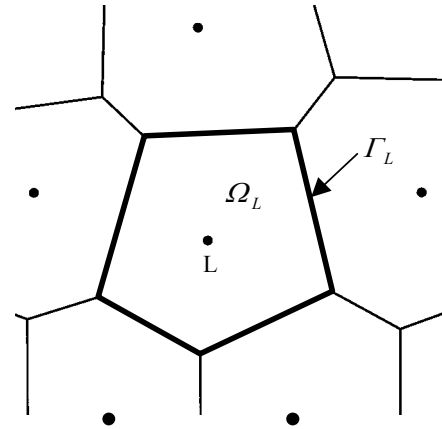


Figure 2 Voronoi Diagram

3. STRAIN SMOOTHING STABILIZATION FOR PATH-DEPENDENT PROBLEMS

Elastoplasticity and frictional contact conditions involved in metal forming analysis are path-dependent. A Lagrangian approach is considered for meshfree discretization, by referencing meshfree shape functions to the material coordinate \mathbf{X} , and transforming the variational equation from the current domain Ω_x to the initial domain Ω_X [10]. The transformation and linearization of the internal energy are given as:

$$\int_{\Omega_x} \delta u_{i,j} \tau_{ij} d\Omega = \int_{\Omega_X} \frac{\partial \delta u_i}{\partial X_k} F_{kj}^{-1} \tau_{ij} J^0 d\Omega \quad (8)$$

$$\int_{\Omega_x} \delta u_{i,j} (C_{ijkl} + T_{ijkl}) \Delta u_{k,l} d\Omega = \int_{\Omega_X} \frac{\partial \delta u_i}{\partial X_m} F_{mj}^{-1} (C_{ijkl} + T_{ijkl}) F_{nl}^{-1} \frac{\partial \Delta u_k}{\partial X_n} J^0 d\Omega \quad (9)$$

where x_i is the spatial coordinate, X_i is the material coordinate, τ_{ij} is the Cauchy stress, $(\cdot)_{,i} \equiv \partial(\cdot)/\partial x_i$, F_{ij} is the deformation gradient, $J^0 = \det(\mathbf{F})$, C_{ijkl} is the material response tensor, and T_{ijkl} is the initial stress tensor. To employ a stabilized conforming nodal integration in the evaluation of stiffness and internal force, the deformation gradient is smoothed by

$$\tilde{F}_{ij}(\mathbf{X}_L) = \frac{I}{A_L^X} \int_{\Gamma_L^X} F_{ij} d\Gamma = \frac{I}{A_L^X} \int_{\Gamma_L^X} (u_i^h N_j) d\Gamma + \delta_{ij} \equiv \tilde{e}_{ij}(\mathbf{X}_L) + \delta_{ij} \quad (10a)$$

$$\tilde{e}_{ij}(\mathbf{X}_L) = \frac{I}{A_L^X} \int_{\Gamma_L^X} (u_i^h N_j) d\Gamma \quad (10b)$$

where N_i , Ω_L^X and Γ_L^X are the surface normal, the nodal representative domain and boundary at node L , respectively, at the initial configuration, and $A_L^X = \int_{\Omega_L^X} d\Omega$. Introducing a Lagrangian

shape function $\Psi_I(\mathbf{X})$ for displacement $u_i^h(\mathbf{X}) = \sum_{I=1}^{NP} \Psi_I(\mathbf{X}) d_{iI}$ into Eq. (10) yields

$$\tilde{e}_{ij}(\mathbf{X}_L) = \sum_I \tilde{b}_{ji}^L d_{iI} \quad (11)$$

where

$$\tilde{b}_{ji}^L = \frac{1}{A_L^X} \int_{\tilde{\Gamma}_L^X} (\Psi_I N_j) d\Gamma \quad (12)$$

For path-dependent problems, the computation of spatial derivatives of displacement is required for stress update. Using the Lagrangian approach, stress update is computed using a smoothed strain increment

$$\Delta \tilde{u}_{i,j}(\mathbf{X}_L) = \Delta \tilde{F}_{ij}(\mathbf{X}_L) \tilde{F}_{kj}^{-1}(\mathbf{X}_L) \quad (13)$$

where $\tilde{F}^{-1}(\mathbf{X}_L)$ is the inverse of $\tilde{F}(\mathbf{X}_L)$ computed by Eq. (10). To introduce smoothed deformation gradient as an independent variable, the mixed variational equation is formulated by an assumed strain method:

$$\delta \Pi(\mathbf{u}, \tilde{\mathbf{F}}) = \int_{\Omega_X} \delta \tilde{F}_{ik} \tilde{F}_{kj}^{-1} \tilde{\tau}_{ij}(\tilde{\mathbf{F}}) \tilde{J}^0(\tilde{\mathbf{F}}) d\Omega - \delta W^{ext}(\mathbf{u}) \quad (14)$$

The resulting stiffness matrix and force vector are:

$$\mathbf{K}_{IJ} = \sum_{L=1}^{NP} \tilde{\mathbf{B}}_I^T(\mathbf{X}_L) \tilde{\mathbf{G}}^T(\mathbf{X}_L) [\mathbf{C}(\tilde{\mathbf{F}}(\mathbf{X}_L)) + \mathbf{T}(\tilde{\mathbf{F}}(\mathbf{X}_L))] \tilde{\mathbf{G}}(\mathbf{X}_L) \tilde{\mathbf{B}}_J(\mathbf{X}_L) \tilde{J}^0(\mathbf{X}_L) A_L \quad (15)$$

$$\mathbf{f}_I^{int} = \sum_{L=1}^{NP} \tilde{\mathbf{B}}_I^T(\mathbf{X}_L) \tilde{\mathbf{G}}^T(\mathbf{X}_L) \tilde{\boldsymbol{\tau}}(\tilde{\mathbf{F}}(\mathbf{X}_L)) \tilde{J}^0(\mathbf{X}_L) A_L \quad (16)$$

$$\tilde{\mathbf{B}}_l(\mathbf{X}_L) = \begin{bmatrix} \tilde{b}_{11}^L & 0 \\ 0 & \tilde{b}_{21}^L \\ \tilde{b}_{21}^L & 0 \\ 0 & \tilde{b}_{11}^L \end{bmatrix} \quad (17)$$

$$\tilde{\mathbf{G}} = \begin{bmatrix} \tilde{F}_{11}^{-1} & 0 & \tilde{F}_{21}^{-1} & 0 \\ 0 & \tilde{F}_{22}^{-1} & 0 & \tilde{F}_{12}^{-1} \\ \tilde{F}_{12}^{-1} & \tilde{F}_{21}^{-1} & \tilde{F}_{22}^{-1} & \tilde{F}_{11}^{-1} \end{bmatrix} \quad (18)$$

$$\tilde{\boldsymbol{\tau}} = \begin{bmatrix} \tilde{\tau}_{11} \\ \tilde{\tau}_{22} \\ \tilde{\tau}_{12} \end{bmatrix} \quad (19)$$

$$\tilde{J}^0 = \det(\tilde{\mathbf{F}}) \quad (20)$$

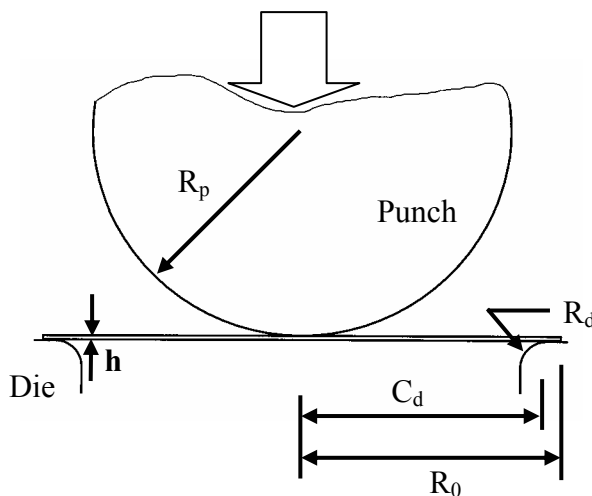
where $\tilde{\mathbf{B}}_l$ is the gradient matrix associated with the smoothed deformation gradient given in Eqns. (10a)-(10b), and $\tilde{\boldsymbol{\tau}}$ is the Cauchy stress calculated using the smoothed strain. Using the Lagrangian approach, the value of $\tilde{\mathbf{B}}_l$ evaluated at the material integration point \mathbf{X}_L does not change with the material deformation, and can therefore be stored and reused for computing $\tilde{\mathbf{F}}(\mathbf{X}_L)$, $\tilde{\mathbf{F}}^{-1}(\mathbf{X}_L)$, \mathbf{K} , and \mathbf{f}^{int} in each load step.

For contact problems, contact constraints are introduced through a penalty-type perturbed Lagrangian formulation [5]. Collocation is employed in the boundary integration of contact stiffness and force terms. A smooth contact surface representation [8] is introduced to generate a smooth contact surface through the nodal locations of the set of contact surface nodes. The smooth surface representation is incorporated into the meshfree formulation to yield a consistent tangent operator for frictional contact problems.

4. NUMERICAL EXAMPLES

4.1 Cylindrical Punch

The problem is described in Fig. 3. A plane-strain sheet metal is stretched by a cylindrical punch. Because of symmetry, only half of the total geometry is modeled. When direct nodal integration is used without stabilization, spurious modes occur in both membrane and transverse directions, as shown in Fig. 4(a). These unstable modes are eliminated in the stabilized conforming nodal integration technique, as illustrated in Fig. 4(b). The load-deflection curves from both integration methods are compared to an analytical membrane solution with various normalized support sizes R (normalized with averaged nodal distance). As shown in Fig 5(a), Direct nodal integration yields poor performance even in linear range, however, the proposed stabilized conforming nodal integration method generates reasonable response compared to the analytical solution as in Fig. 5(b). Notice that the analytical solution does not consider the necking phenomenon which is captured in the simulation.



Geometry parameters

$$R_p = 50.8 \text{ mm}$$

$$h = 1.0 \text{ mm}$$

$$R_d = 6.35 \text{ mm}$$

$$C_d = 59.18 \text{ mm}$$

$$R_0 = 61.30 \text{ mm}$$

Material properties

$$\text{Young's Modulus } E = 69 \text{ GPa}$$

$$\text{Poisson's ratio } \nu = 0.3$$

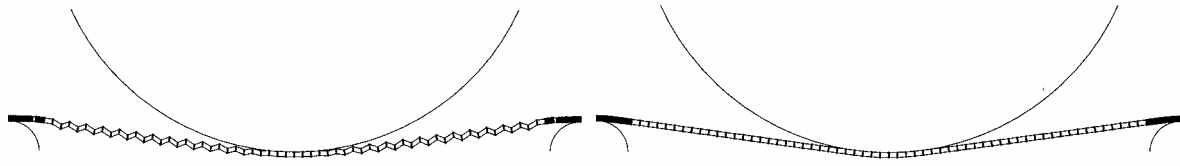
Isotropic hardening:

$$\sigma_y(\bar{\epsilon}^p) = 589(10^{-4} + \bar{\epsilon}^p)^{0.216}$$

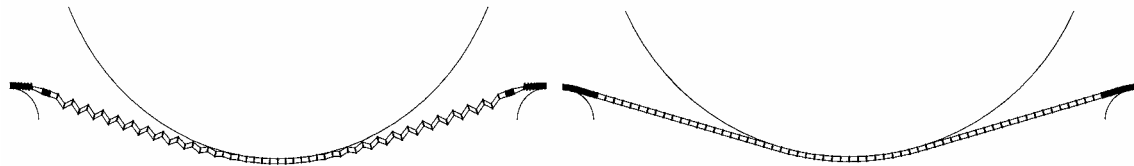
σ_y = yield stress

$\bar{\epsilon}$ = effective plastic strain

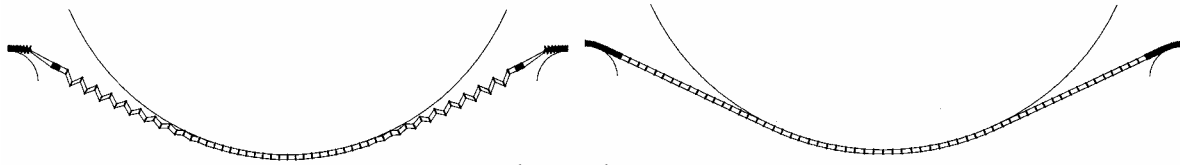
Figure 3 Cylindrical punch problem statement



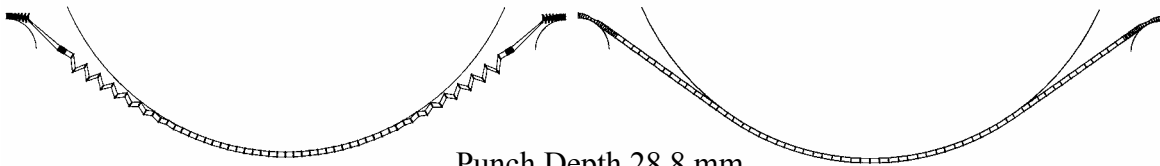
Punch Depth 7.5 mm



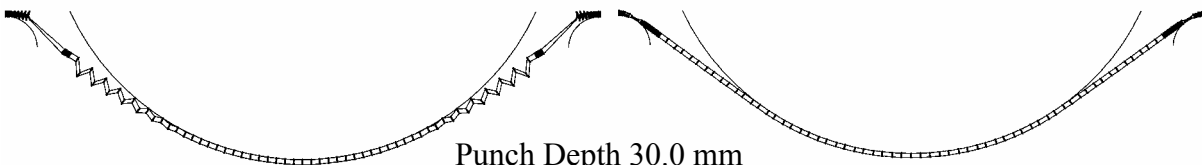
Punch Depth 15.0 mm



Punch Depth 22.5 mm



Punch Depth 28.8 mm



Punch Depth 30.0 mm

(a) Direct nodal integration

(b) Stabilized conforming nodal integration

Figure 4 Meshfree analysis of cylindrical punch without and with stabilization

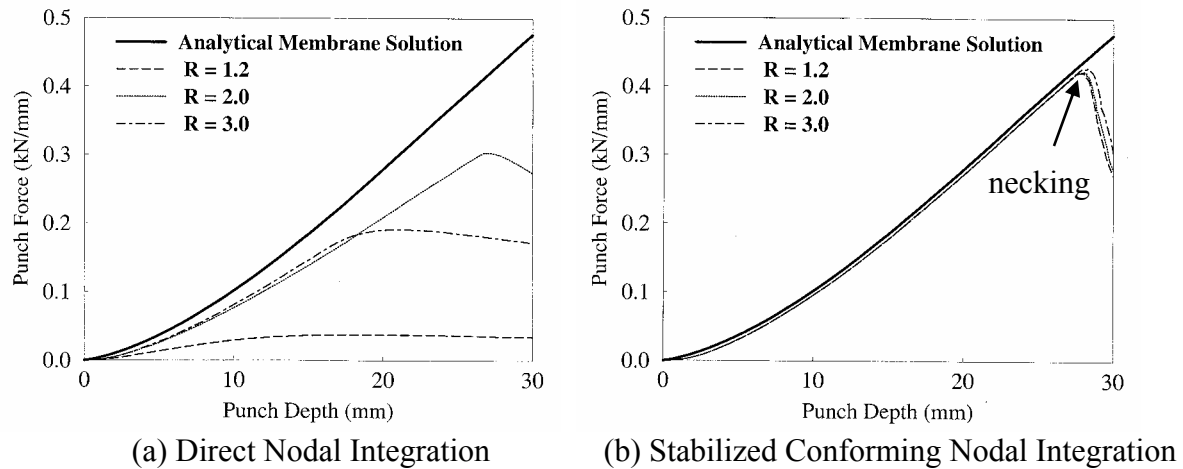


Figure 5 Comparison of the cylindrical punch load-displacement response

4.2 Necking

An axisymmetric elastoplastic bar is subjected to an axial prescribed displacement as shown in Fig. 6. A geometric imperfection at the center of the rod is introduced, for which a quarter of the geometry is modeled. The displacement solution from direct nodal integration exhibits spatial oscillation in both the axial and transverse directions. Non-physical necking deformation occurs near the interface of the regions that exhibit substantial difference in nodal density (Fig. 6(a)). Spatial instability and non-physical necking are suppressed and corrected by the stabilized conforming nodal integration (Fig. 6(b)). Good agreement between experimental data and the stabilized conforming nodal integration solution is shown in Fig. 7.

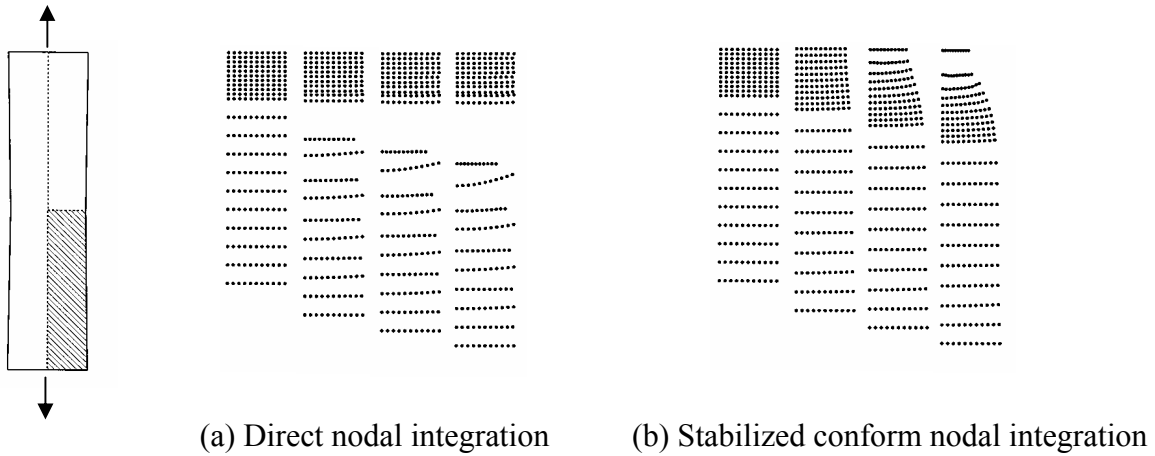


Figure 6 Necking analysis by (a) direct nodal integration and (b) stabilized conforming nodal integration

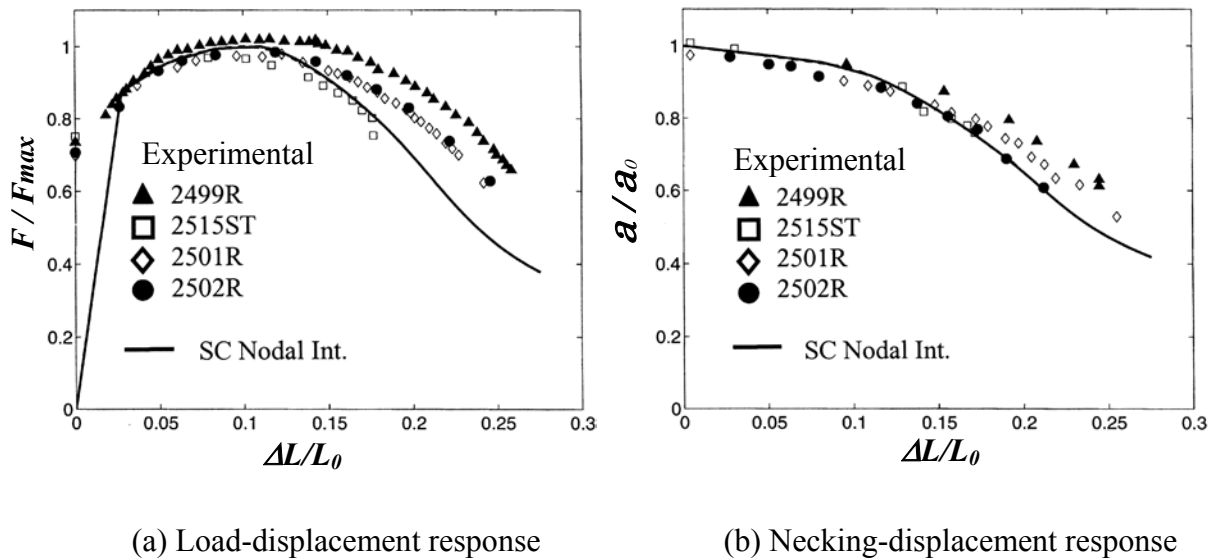


Figure 7 Comparison of meshfree solution with stabilized conforming nodal integration with experimental data [2] (F = axial force, L_0 = original axial length, ΔL = incremental axial length, a_0 = original width, and a = deformed width)

4.3 Springback in Flanging

A straight flanging operation and its springback behavior of a sheet metal are simulated, and the predicted springback angle is compared with experimental data reported in [9]. The geometric parameters of a flanging operation are shown in Fig. 8. Results obtained using an meshfree discretization of 5x131 nodes with three shape function support sizes $r=1.2, 2.0,$ and 3.0 are shown in this paper.

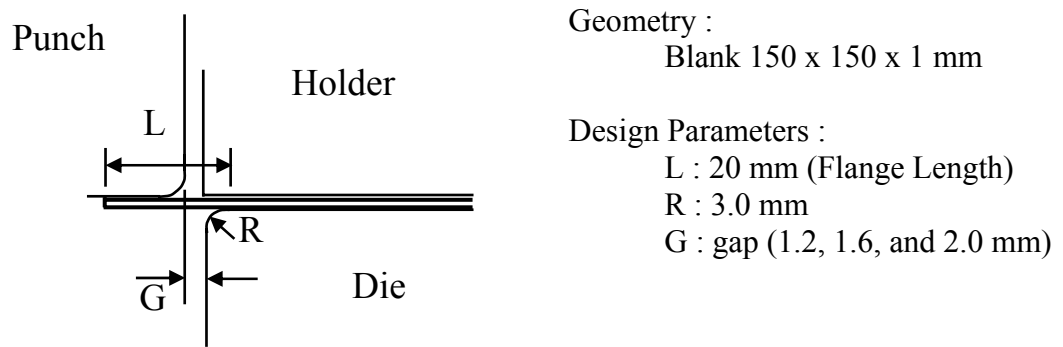


Figure 8 Problem description and geometry parameters

The predicted angles of springback for three gap dimensions $G=1.2, 1.6,$ and 2.0 are compared with experimental data [9] as shown in Fig. 9. The meshfree results show good agreement with experimental data, where the springback angle increases as the gap dimension increases. The results also demonstrate that the meshfree discretization with larger shape function support size provides a slightly better agreement with the experimental data. Typical flanging progressive deformations and shape function normalized support size of 2.0 are shown in Fig. 10.

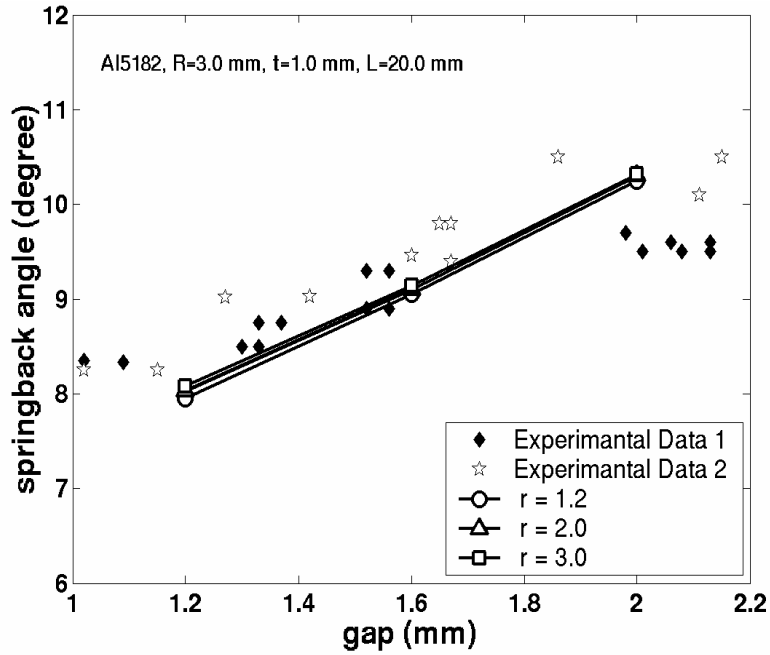


Figure 9 Comparison of meshfree solution with experimental measurement [9] of springback angles

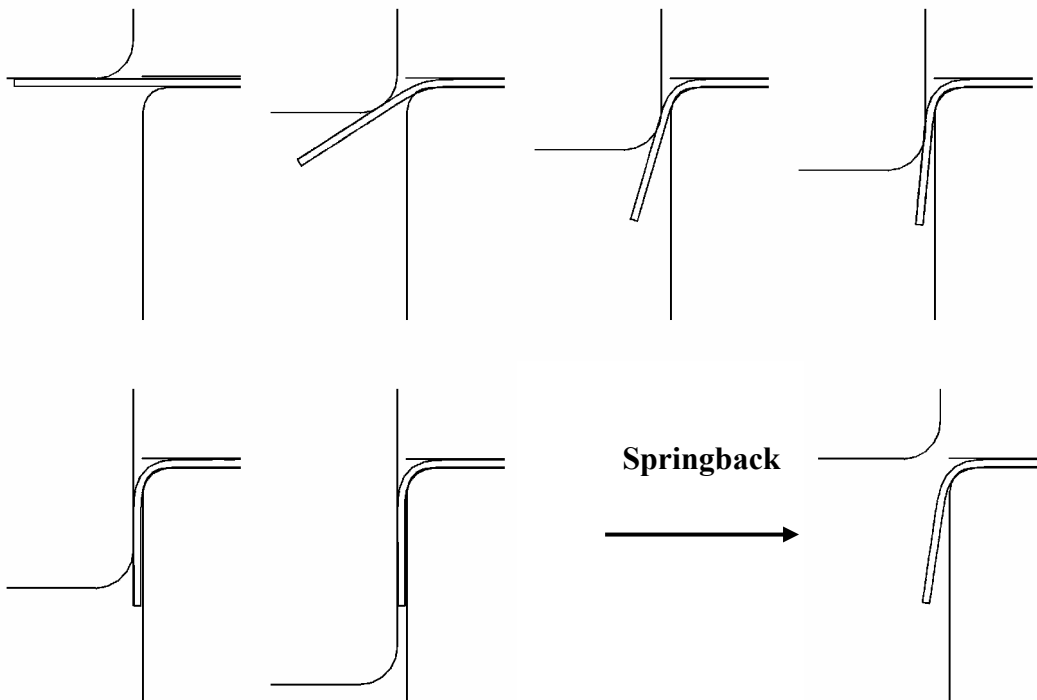


Figure 10 Deformation and springback of the flanging operation simulated by meshfree method

4.4 Extrusion

A 3D elastoplastic cylindrical billet is extruded through a rigid circular die as shown in Fig 11. Extrusion is achieved by prescribing displacements at the top end of the billet. Because of symmetry, only one quarter of the total billet is modeled by 711 particles. Both the Gauss integration method and the proposed stabilized conforming nodal integration (SCNI) were used in the analysis for comparison. The SCNI yields results very similar to that of the Gauss integration, and therefore only the deformation obtained by SCNI is shown in Fig. 12. The CPU time for SCNI is only 10% of that required in the Gauss integration method.

Geometry

Billet: radius = 40 mm
length = 60 mm
Die: external radius = 40 mm
internal radius = 20 mm
height = 110 mm.

Material properties

Young's Modulus $E = 100$ GPa
Poisson's ratio $\nu = 0.3$
Isotropic hardening:
 $\sigma_y(\bar{\epsilon}^p) = 300 + 200 \bar{\epsilon}^p$ MPa
 σ_y = yield stress
 $\bar{\epsilon}$ = effective plastic strain

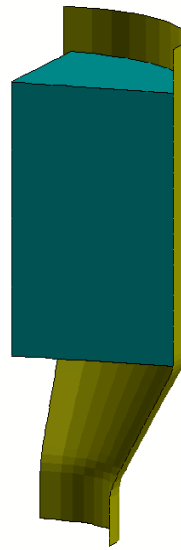


Figure 11 Geometry of extrusion problem

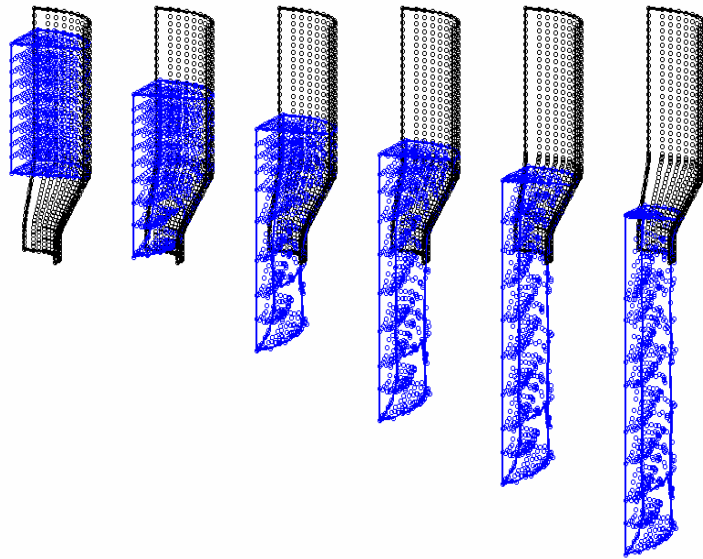


Figure 12 Extrusion processes modeled by stabilized conforming nodal integration

5. CONCLUSION

A stabilization technique for nodally integrated Galerkin meshfree methods for path-dependent problems has been developed to enhance computational efficiency in meshfree analysis. The proposed strain smoothing in the deformation gradient results in a smoothed gradient matrix that meets the linear exactness in the Galerkin approximation and it also serves as a stabilization mechanism. It has shown that a severe oscillation in displacement occurs in the solution using the direct nodal integration was effectively suppressed using the proposed stabilized conforming nodal integration. In this approach, the formation of the discrete equations was accelerated by an order of magnitude compared to the Gauss integration method. Substantial memory savings were achieved particularly, for path-dependent materials. Several metal forming problems were analyzed to examine the effectiveness of the proposed method.

REFERENCES

1. C. A. M. Duarte and J. T. Oden, A h-p Adaptive Method Using Clouds, *Comput. Meth. Appl. Mech. Engng.* 139 (1996) 237-262.
2. D. M. Norris, B. Moran, Jr., J. K. Scudder and D. F. Quinones, A Computer Simulation of the Tensile Test, *J. Meth. Phys. Solids*, 16 (1978) 1-19.
3. I. Babuska and J. M. Melenk, The Partition of Unity Method, *Int. J. Numer. Meth. Eng.* 40 (1997) 727-758.
4. J. Dolbow, and T. Belytschko, Numerical Integration of Galerkin weak Form in Meshfree Methods, *Computational Mechanics*, 23 (1999) 219-230.
5. J. S. Chen, C. Pan, C. M. O. L. Roque and H. P. Wang, A Lagrangian Reproducing Kernel Particle Method for Metal Forming Analysis, *Computational Mechanics*, 22 (1998) 289-307.

6. J. S. Chen, C. Pan, C. T. Wu and W. K. Liu, Reproducing Kernel Particle Methods for Large Deformation Analysis of Nonlinear Structures, *Comput Meth. Appl. Mech. Engng.* 139 (1996) 195-227.
7. J. S. Chen, C. T. Wu, S. Yoon and Y. You, Stabilized Conforming Nodal Integration for Galerkin Meshfree Methods, *Int. J. Numer. Meth. Eng.*, 50 (2001) 435-466.
8. J. S. Chen and H. P. Wang, Meshfree Smooth Contact Formulation, to submit, *Comput Meth. Appl. Mech. Engng.*(2001)
9. N. Song, D. Qian, J. Cao, W. K. Liu and S. Li, S. Effective Models for Prediction of Springback in Flanging, *ASME J. Eng. Mater. Technol.* 123 (2001) 456-461.
10. T. Belytschko, Y. Y. Lu and L. Gu, Element-Free Galerkin Methods, *Int. J. Numer. Meth. Eng.* 37 (1994) 229-256.
11. W. K. Liu, S. Jun, and Y. F. Zhang, Reproducing Kernel Particle Methods, *Int. J. Numer. Meth. Fluids.* 20 (1995) 1081-1106.